

Local and Global Structural Health Monitoring via Stochastic Functional Time Series Methods: A Critical Assessment and Comparison

Shabbir Ahmed*, Peiyuan Zhou†, Seth Zager‡, and Fotis Kopsaftopoulos§
Rensselaer Polytechnic Institute, Troy, NY, 12180

In the arena of structural health monitoring (SHM), ultrasonic guided wave-based and vibration-based damage detection and identification methods constitute two seemingly distinct approaches, oftentimes treated separately. Guided-waves-based methods are typically used for “local” damage diagnosis due to their increased sensitivity while vibration-based methods are based on the premise that damage has an impact on the global structural dynamic response, therefore are typically used for tackling “global” damage diagnosis. In this work, we present the comparison and critical assessment of the two state-of-the-art time-series-based methods, a local method based on guided waves and a global method based on structural vibrations, via a series of progressive damage analysis (PDA) numerical simulations and experiments on a composite unmanned aerial vehicle (UAV) wing structure. At first, a finite element model is established for progressive damage analysis on a composite plate fitted with piezoelectric sensors/actuators. Then, ultrasonic guided wave signals are generated and collected in a pitch-catch configuration as damage progression occurs while the low-frequency vibratory response and modal analysis results are also generated to allow the comparison of the local and global diagnostic methods. Next, both methods are implemented and assessed on a composite UAV wing structure, outfitted with accelerometers and piezoelectric sensors, to collect active-sensing pitch-catch ultrasonic and vibration response signals under different damage locations and magnitudes. The diagnostic methods presented are based on: (i) stochastic functional series time-varying autoregressive (FS-TAR) models to represent the ultrasonic guided wave propagation and enable the subsequent FS-TAR model-based local damage detection and identification tasks, and (ii) functionally pooled autoregressive models with exogenous excitation (FP-ARX) models to enable the vibration-based global damage diagnosis. It is shown that by incorporating a local guided wave-based damage diagnosis scheme within the global vibration-based damage detection and identification framework, both the sensitivity and robustness for detecting and identifying (localizing and quantifying) minor damage can be significantly increased.

I. Introduction

The next generation of intelligent aerospace structures and aerial vehicles will be able to “feel,” “think,” and “react” in real-time based on high-resolution state-sensing, awareness, and self-diagnostic capabilities. They will be able to sense and observe phenomena at unprecedented lengths and time scales allowing for real-time optimal control and decision-making, significantly improved performance, adaptability, autonomous operation, increased safety, reduced mission and maintenance costs, and complete life-cycle monitoring and management. In order to help achieve autonomous operation with state-awareness capabilities, an integrated robust structural health monitoring (SHM) system may play an important role.

SHM refers to the process of implementing a damage diagnosis scheme for aerospace, civil and mechanical structures. SHM systems employ distributed, permanently installed sensors at certain structural regions and employ diagnostic and prognostic algorithms to extract meaningful health information from the sensing data [1–4]. Depending on the monitored area of the structure, SHM methods may be classified as local or global. When the diagnostic approach targets a specific area or part of a structure, it is referred to as a local or “hotspot” monitoring method. Acousto-ultrasonic

*Graduate Research Assistant, Department of Mechanical, Aerospace, and Nuclear Engineering; ahmeds6@rpi.edu.

†Graduate Research Assistant, Department of Mechanical, Aerospace, and Nuclear Engineering; zhoup2@rpi.edu

‡Graduate Research Assistant, Department of Mechanical, Aerospace, and Nuclear Engineering; zagers@rpi.edu

§Assistant Professor, Department of Mechanical, Aerospace, and Nuclear Engineering; kopsaf@rpi.edu; AIAA Senior Member.

guided waves, eddy current, and electromechanical impedance (EMI) based methods fall under the category of local methods [5–8]. On the other hand, when a diagnostic method is based on the hypothesis that damage can be detected when it affects the global dynamic response of the structure, a larger area or substructure, or component, it is referred to as a global SHM method. Vibration-based methods fall under this category. They are based on the principle that small changes in the structure cause discrepancies in its vibration response which may be detected and associated with a specific type/size/location of the damage.

Within the family of local SHM approaches, ultrasonic guided wave-based methods constitute a prominent class of highly sensitive damage diagnosis schemes. Ultrasonic guided waves are elastic stress waves that propagate through thin structures [7, 9]. In non-dissipative media, such as metals, these waves can propagate long distances, therefore, enabling various diagnostic methods. Such waves can be easily generated and recorded with the help of Lead-Zirconate-Titanate (PZT) transducers. Features of the guided wave signals, such as specific mode amplitude, signal energy, and/or time of flight can be used to formulate appropriate metrics (usually known as damage indices, i.e., DIs) to enable damage diagnosis [10–12]. Although these methods are highly sensitive to tiny structural changes, defects, or damage, they are equally susceptible to environmental and operational conditions (EOC). The effects of EOC can oftentimes mask the presence of damage or give a false indication of damage. In addition, an array of dense sensor networks may be required to properly detect and identify damage using guided waves for different actuator-sensor propagation paths. When it comes to the generation of guided waves, various tone bursts or narrow-band signals are usually employed, therefore exciting a narrow frequency band centered around the actuation frequency. This type of actuation may contain limited damage-related information as specific structural modes are excited that may have different sensitivity to potential damage and/or defect types.

On the other hand, within the global family of SHM approaches, vibration-based methods may offer advantages over guided wave-based methods while also facing specific challenges [13]. These methods exhibit increased robustness in the face of EOCs and can operate even with a limited number of sensors. A low-frequency random white noise excitation is usually employed which results in the identification of the vibratory modes of the structure within the frequency bandwidth of interest. In addition, ambient excitation can also be employed, as this is the case in many aerospace, mechanical, and civil structures. As a result, the received response signals may contain enriched damage-related information when it comes to the dynamic content of the structure [13–16]. However, vibration-based methods may suffer from reduced sensitivity to smaller damage and/or defects, as they may not significantly affect the global dynamic vibration response of the structure. As damage grows in size and/or magnitude, the compliance of the structure increases, therefore its vibration response changes and damage becomes detectable as it starts affecting the structural dynamics. Spada et al. [17] have proposed a global-local model for three dimensional guided wave scattering for rail flaw detection. In this approach, a semi-analytical finite element (SAFE) model was used for the global portion of the structure, and a full finite element (FE) discretization for the local portion of the structure containing discontinuities. Zhu et al. [18] investigated fatigue crack detection using ultrasonic guided waves with the presence of low-frequency background vibrations. Several researchers have investigated the interaction between low-frequency vibration and high-frequency ultrasonic wave propagation for detecting fatigue crack growth in structural components [19–21]. However, the investigation and integration of low-frequency vibration-based global monitoring and guided wave-based local monitoring have not been previously addressed within a unified stochastic time series modeling and diagnostic approach.

In this study, two different SHM approaches, namely an ultrasonic guided wave-based and a vibration-based method, are investigated, assessed, and combined within a unified stochastic time series modeling and diagnostic framework with respect to tackling damage detection and identification/quantification. First, a progressive damage analysis (PDA) method for composite structures is established using a finite element model to represent damage propagation within a carbon-fiber composite plate. The PDA method can model increasing damage, both in terms of the affected area and severity, in a composite laminate via the proper modeling of the stiffness loss of the material. The resulting model with the degraded material properties reflecting damage of different severity is then used for the multi-physics simulation of ultrasonic wave propagation via the additional modeling of a network of piezoelectric (PZT) actuators/sensors. In addition, the global dynamic response of the composite plate is also obtained via a series of FEM simulations in the frequency domain. Next, the complete experimental assessment of the local, ultrasonic guided wave, and global, vibration-based, methods are presented on a composite wing. In order to integrate the guided wave (local) [9] and vibration-based (global) [3] damage diagnosis schemes, stochastic functional time series models are used to represent both the ultrasonic wave propagation and low-frequency vibration response of the wing. The overall idea is that the local approach can detect small damage that does not affect the global dynamic response, therefore the global approach might miss. Moreover, as damage propagates, the robustness of the quantification can be enhanced by combining both

local and global approaches. The goal of this work is to demonstrate and assess the effectiveness and robustness of the combined local-global methods both numerically and experimentally.

The paper is organized in the following order: first, the background theory and analysis methods are presented. Then, the simulation and experimental setups, and data generation processes are outlined. Next, the results of the local and global damage diagnosis methods as well as the PDA results are presented. Finally, the key points are summarized in the conclusions.

II. Theoretical Background

A. Progressive Damage Analysis

In order to study progressive damage analysis (PDA) of composite plates, a user defined material model (UMAT) subroutine in Abaqus has been used. Abaqus UMAT lets the user define a damage criterion and a damage progression model in a FORTRAN subroutine to be implemented into a finite element model (FEM). The damage criterion determines which elements in the model are considered damaged, and the damage progression model determines how the material properties of the damaged elements change throughout the simulation. The model in this study was composed of a two-dimensional shell elements to reduce the computational cost. While using a user defined material, the user must specify a constitutive model in the UMAT code. For a two-dimensional model, the following constitutive relationship was utilized

$$\{\sigma\} = \begin{Bmatrix} \sigma_{11} \\ \sigma_{22} \\ \sigma_{12} \end{Bmatrix} = \begin{bmatrix} C_{11}^0 & C_{12}^0 & 0 \\ C_{21}^0 & C_{22}^0 & 0 \\ 0 & 0 & C_{44}^0 \end{bmatrix} \begin{Bmatrix} \varepsilon_{11} \\ \varepsilon_{22} \\ \gamma_{12} \end{Bmatrix} = [C^0] \{\varepsilon\} \quad (1)$$

$$C_{11}^0 = \frac{E_{11}}{1 - \nu_{12}\nu_{21}}; \quad C_{22}^0 = \frac{E_{22}}{1 - \nu_{12}\nu_{21}}; \quad C_{12}^0 = C_{21}^0 = \frac{\nu_{12}E_{22}}{1 - \nu_{12}\nu_{21}} = \frac{\nu_{21}E_{11}}{1 - \nu_{12}\nu_{21}}; \quad C_{44}^0 = G_{12} \quad (2)$$

A damage criterion needs to be specified in the UMAT code for PDA. The damage criterion is a set of equations that are included in the UMAT code that determines which elements in the model are damaged. The equations use the elemental components of stress as inputs and the material properties of the composite as constants. The damage criterion utilized for the PDA in this study was the Tsai-Wu Damage Criterion. Tsai-Wu was chosen due to its ability to account for interactions between stress components while being computationally inexpensive. For a two-dimensional model, the Tsai-Wu failure criterion takes the form of the following equations:

$$\begin{aligned} \phi &= \phi_1 + \phi_2 + \phi_3 \\ \phi_1 &= F_1\sigma_{11} + F_{11}(\sigma_{11})^2 + F_{12}\sigma_{11}\sigma_{22} \\ \phi_2 &= F_2\sigma_{22} + F_{22}(\sigma_{22})^2 + F_{12}\sigma_{11}\sigma_{22} \\ \phi_3 &= F_{66}(\sigma_{12})^2 \end{aligned} \quad (3)$$

The constants in these equations are derived from the material properties and are defined as

$$\begin{aligned} F_1 &= \frac{1}{X_T} - \frac{1}{X_C}; & F_2 &= \frac{1}{Y_T} - \frac{1}{Y_C}; \\ F_{11} &= \frac{1}{X_T X_C}; & F_{22} &= \frac{1}{Y_T Y_C}; \\ F_{66} &= \frac{1}{(S_{12})^2}; & F_{12} &= -\frac{1}{2} \frac{1}{\sqrt{X_T X_C Y_T Y_C}}; \end{aligned}$$

For each iteration in the PDA simulation, each node's value of ϕ is solved. If that value exceeds 1, the node is considered damaged. Once the damage is detected, the damage progression model determines what happens to the elemental stiffness matrix of each damaged element. As with the damage criterion, there have been multiple methods developed for damage progression modeling. This study utilized a ply-discounting approach for its simplicity and computational efficiency. In the ply-discounting method, each term in the elemental stiffness matrix is multiplied by a degradation factor β . This factor ranges in value from 1 for completely undamaged elements to 0 for elements with no

remaining stiffness due to damage. The UMAT code multiplies the terms in the stiffness matrix using the following equation:

$$\{\sigma\} = \beta [C^0] \{\varepsilon\} \quad (4)$$

The value of the damage factor β is determined by how many simulation iterations each element has been considered damaged. Once the Tsai-Wu failure criterion determines that an element is damaged, its damage factor is decreased and continues to decrease for each of the remaining iterations of the simulation. Using this method, the PDA can output each element's value of β at the end of the simulation. This output represents the remaining stiffness in all elements. The user can then use this output as the initial conditions of a different simulation to model a damaged structure.

B. Functional Series Time-Varying Autoregressive (FS-TAR) Model

In order to perform local damage diagnosis, ultrasonic guided waves are used in this study. Guided waves are inherently non-stationary due to their time-dependent (evolutionary) characteristics. Deterministic parameter evolution TAR representation imposes a deterministic structure upon the time evolution of their parameters [22–24]. This is achieved by postulating model parameters as deterministic functions of time, belonging to specific functional subspaces. Such representations are referred to as FS-TAR models. Their AR parameters, as well as the innovation's standard deviation, are all expanded within properly selected functional subspaces defined as

$$\mathcal{F}_{AR} \triangleq \{G_{b_a(1)}[t], G_{b_a(2)}[t] \dots G_{b_a(p_a)}[t]\} \quad (5)$$

$$\mathcal{F}_{\sigma_e} \triangleq \{G_{b_s(1)}[t], G_{b_s(2)}[t] \dots G_{b_s(p_s)}[t]\} \quad (6)$$

In these expressions, the “ \mathcal{F} ” designates the functional subspace of the indicating quantity and $G_j[t]$ a set of orthogonal basis functions selected from a suitable family (such as Chebyshev, Legendre, and other polynomials, trigonometric, wavelet or other functions). The AR and standard deviation subspace dimensionalities are indicated as p_a and p_s , respectively, while, the indices $b_a(i)(i = 1, \dots, p_a)$ and $b_s(i)(i = 1, \dots, p_s)$ designate the specific basis functions of a particular family that are included in each subspace. The time-dependent AR and innovations standard deviations of an FS-TAR(na) $_{[p_a, p_s]}$ representation may thus be expressed as

$$y[t] + \sum_{i=1}^{na} a_i[t] \cdot y[t-i] = e[t], \quad \text{with } e[t] \sim \text{iid } \mathcal{N}(0, \sigma_e^2[t]) \quad (7)$$

$$a_i[t] \triangleq \sum_{j=1}^{p_a} a_{i,j} \cdot G_{b_a(j)}[t] \quad \sigma_e[t] \triangleq \sum_{j=1}^{p_s} s_j \cdot G_{b_s(j)}[t] \quad (8)$$

with $a_{i,j}$ and s_j designating the AR and innovations standard deviation coefficients of projection. An FS-TAR model is thus parametrized in terms of its projection coefficients $a_{i,j}$ and s_j . The coefficients of projection vector

$\boldsymbol{\vartheta} = [a_{1,1} \dots a_{1,p_a} \dots a_{na,1} \dots a_{na,p_a}]^T_{[napax1]}$ has to be estimated from the available data.

The model identification problem for FS-TAR is usually distinguished into two subproblems: (i) *parameter estimation* and (ii) *model structure selection*. For a detailed review of parameter estimation and model structure selection methods see [22, 24].

The maximum likelihood (ML) estimation of the coefficients of projection vector $\boldsymbol{\vartheta}$ may be obtained through the maximization of the log-likelihood function, which for the FS-TAR model and under the Gaussian assumption for the innovations sequence may be given as

$$\ln \mathcal{L}(\boldsymbol{\vartheta}, \sigma_e | y^N) = -\frac{N}{2} \ln 2\pi - \frac{1}{2} \sum_{t=1}^N \left(\ln \sigma_e^2[t] + \frac{e^2[t, \boldsymbol{\vartheta}]}{\sigma_e^2[t]} \right) \quad (9)$$

with $\sigma_e = [\sigma_e^2[1], \dots, \sigma_e^2[N]]^T$ constituting a nuisance parameter vector of high dimensionality while $\boldsymbol{\vartheta}$ is a parameter vector of low dimensionality. In such cases, the nuisance parameter vector may be profiled out from the log-likelihood function by considering the conditional maximum likelihood (CML) estimate of $\widehat{\sigma}_e$ for known $\boldsymbol{\vartheta}$ and substituting it into Equation 9. Toward this end,

$$\frac{\partial \ln \mathcal{L}}{\partial \sigma_e^2[t]} = 0 \quad \Rightarrow \quad -\frac{1}{2} \cdot \left[\frac{1}{\sigma_e^2[t]} - \frac{e^2[t, \boldsymbol{\vartheta}]}{\sigma_e^4[t]} \right] \quad \Rightarrow \quad \widehat{\sigma}_e^2[t] = e^2[t, \boldsymbol{\vartheta}] \quad (10)$$

Then it follows that

$$\widehat{\boldsymbol{\vartheta}} = \arg \max_{\boldsymbol{\vartheta}} \{ \ln \mathcal{L}(\boldsymbol{\vartheta}, \widehat{\sigma}_e | y^N) \} = \arg \max_{\boldsymbol{\vartheta}} \left[-\frac{1}{2} \sum_{t=1}^N \ln e^2[t, \boldsymbol{\vartheta}] \right] \quad (11)$$

$\widehat{\boldsymbol{\vartheta}}$ is actually a pseudo-likelihood estimator which actually leads to the same point estimate with the original ML estimator of $\boldsymbol{\vartheta}$ and σ_e . Once the FS-TAR coefficients of projection vector $\boldsymbol{\vartheta}$ are estimated (which are constants), the time-varying parameter vector $\boldsymbol{\theta}[t] = [a_1[t], a_2[t] \cdots a_{na}[t]]_{na \times 1}$ can be estimated by multiplying with the basis functions as shown in Equation 8. The estimation of the innovation's standard deviation coefficients of projection may be achieved as described in [25]. For details of the FS-TAR model structure selection see [22, 25, 26].

In this study, the local damage detection and identification have been performed using coefficients of projection which provide damage diagnosis results similar to the AR models [12].

1. Coefficients of Projection-based Damage Diagnosis

In this method, damage detection and identification of a structure can be based on a characteristic quantity $Q = f(\boldsymbol{\vartheta})$, which is a function of the AR coefficients of projection vector $\boldsymbol{\vartheta}$ of the FS-TAR model. Note that coefficients of projection are constants and do not vary with time. Let $\widehat{\boldsymbol{\vartheta}}$ designate a proper estimator of the coefficients of projection vector $\boldsymbol{\vartheta}$. For a sufficiently long signal, the estimator is (under mild assumptions) Gaussian distributed with a mean equal to its true value $\boldsymbol{\vartheta}$ and a certain covariance $\mathbf{P}_{\boldsymbol{\vartheta}}$, hence $\widehat{\boldsymbol{\vartheta}} \sim \mathcal{N}(\boldsymbol{\vartheta}, \mathbf{P}_{\boldsymbol{\vartheta}})$. Damage diagnosis is then based on testing for statistically significant changes in the coefficients of projection vector $\boldsymbol{\vartheta}$ between the nominal and current state of the structure through the following hypothesis testing problem:

$$H_0 : \delta\boldsymbol{\vartheta} = \boldsymbol{\vartheta}_o - \boldsymbol{\vartheta}_u = 0 \quad \text{null hypothesis--healthy structure} \quad (12)$$

$$H_1 : \delta\boldsymbol{\vartheta} = \boldsymbol{\vartheta}_o - \boldsymbol{\vartheta}_u \neq 0 \quad \text{alternative hypothesis -- damaged structure} \quad (13)$$

The difference between the two parameter vector estimators follows Gaussian distribution, that is, $\delta\widehat{\boldsymbol{\vartheta}} = \widehat{\boldsymbol{\vartheta}}_o - \widehat{\boldsymbol{\vartheta}}_u \sim \mathcal{N}(\delta\widehat{\boldsymbol{\vartheta}}, \delta\mathbf{P}_{\boldsymbol{\vartheta}})$, with $\delta\boldsymbol{\vartheta} = \boldsymbol{\vartheta}_o - \boldsymbol{\vartheta}_u$ and $\delta\mathbf{P} = \mathbf{P}_o + \mathbf{P}_u$, where $\mathbf{P}_o, \mathbf{P}_u$ designate the corresponding covariance matrices. Under the null (H_0) hypothesis $\delta\widehat{\boldsymbol{\vartheta}} = \widehat{\boldsymbol{\vartheta}}_o - \widehat{\boldsymbol{\vartheta}}_u \sim \mathcal{N}(0, 2\mathbf{P}_o)$ and the quantity

$$Q = \delta\widehat{\boldsymbol{\vartheta}}^T \cdot \delta\mathbf{P}^{-1} \cdot \delta\widehat{\boldsymbol{\vartheta}}, \quad \delta\mathbf{P} = 2\mathbf{P}_o \quad (14)$$

follows a χ^2 distribution with $d = \dim(\boldsymbol{\vartheta})$ (parameter vector dimensionality) degrees of freedom. The associated covariance matrix for the estimated coefficients of projection vector $\boldsymbol{\vartheta}$ can be obtained as [25]:

$$\begin{aligned} \mathbf{P}_{\boldsymbol{\vartheta}} &= \frac{1}{N} \cdot \left\{ \frac{1}{N} \sum_{t=1}^N \frac{\boldsymbol{\phi}_A[t] \cdot \boldsymbol{\phi}_A^T[t]}{(\mathbf{g}_s^T[t] \cdot \widehat{\mathbf{s}}^{ML})^2} \right\}^{-1} \cdot \left\{ \frac{1}{N} \sum_{t=1}^N \frac{\sigma_e^2[t] \cdot \boldsymbol{\phi}_A[t] \cdot \boldsymbol{\phi}_A^T[t]}{(\mathbf{g}_s^T[t] \cdot \widehat{\mathbf{s}}^{ML})^4} \right\} \\ &\quad \left\{ \frac{1}{N} \sum_{t=1}^N \frac{\boldsymbol{\phi}_A[t] \cdot \boldsymbol{\phi}_A^T[t]}{(\mathbf{g}_s^T[t] \cdot \widehat{\mathbf{s}}^{ML})^2} \right\}^{-1} \end{aligned} \quad (15)$$

with

$$\boldsymbol{\phi}_A^T[t] \triangleq [-G_{b_a(1)}[t] \cdot y[t-1], \dots, b_a(pa)[t] \cdot y[t-na]]_{(na \cdot pa) \times 1}^T \quad (16)$$

As the covariance matrix \mathbf{P}_o corresponding to the healthy structure is unavailable, its estimated version $\widehat{\mathbf{P}}_o$ is used. It is to be noted here that, when $\widehat{\mathbf{P}}_o$ is estimated from the data, the quantity Q in Equation 14 follows a Hotelling's \mathcal{T}^2 distribution, which in turn, can be related to the Fisher's \mathcal{F} distribution. When $N \rightarrow \infty$, the \mathcal{F} distribution converges to χ^2 distribution. Then the following test is constructed at the α (type I) risk level:

$$Q \leq \chi^2_{1-\alpha}(d) \implies H_0 \text{ is accepted} \quad (17)$$

$$\text{Else} \implies H_1 \text{ is accepted} \quad (18)$$

where, $\chi^2_{1-\alpha}(d)$ designates the χ^2 distribution's $(1 - \alpha)$ critical points. Damage identification may be based on multiple hypothesis testing problems comparing the parameter vector $\widehat{\boldsymbol{\vartheta}}_u$ belonging to the current structural state to those corresponding to different damage types $\widehat{\boldsymbol{\vartheta}}_A, \widehat{\boldsymbol{\vartheta}}_B, \dots$

C. Vector-Dependent Functionally Pooled (VFP) Global Model

The global, vibration-based SHM method presented in this work is based on Vector-dependent Functionally Pooled (VFP) AutoRegressive with eXogenous excitation (ARX) models. The VFP-ARX representation belongs to the recently introduced broader class of stochastic FP models, which makes use of functional data pooling techniques for combining and optimally treating (as one entity) the data obtained from various experiments corresponding to different structural states, and statistical techniques for model estimation [3, 27].

The modeling of a specific damage topology via a VFP-ARX model involves consideration of all admissible damage magnitudes occurring at predetermined locations on a specific part of the structure. For this reason, a total of $M_1 \times M_2$ experiments are performed, with M_1 and M_2 designating the number of experiments under the various damage magnitudes and locations, respectively. Each experiment is characterized by a specific damage magnitude k^1 and a specific damage location k^2 , with the complete series covering the required range of each variable, say $[k_{min}^1, k_{max}^1]$ and $[k_{min}^2, k_{max}^2]$, via the discretizations $\{k_1^1, k_2^1, \dots, k_{M_1}^1\}$ and $\{k_1^2, k_2^2, \dots, k_{M_2}^2\}$ (it is tacitly assumed, without loss of generality, that the healthy structure corresponds to $k^1 = 0$). For the identification of a model corresponding to a specific damage topology, the vector operating parameter \mathbf{k} containing the damage magnitude and damage location components, is defined as:

$$\mathbf{k} \triangleq [k_i^1, k_j^2]^T \iff k_{i,j}, \quad i = 1, 2, \dots, M_1, \quad j = 1, 2, \dots, M_2$$

with $k_{i,j}$ designating the state of the structure corresponding to the i -th damage magnitude and j -th damage location. This procedure yields a pool of excitation response signal pairs (each of length N):

$$x_{\mathbf{k}}, y_{\mathbf{k}} \text{ with } t = 1, 2, \dots, N \quad k^1 \in \{k_1^1, k_2^1, \dots, k_{M_1}^1\} \quad k^2 \in \{k_1^2, k_2^2, \dots, k_{M_2}^2\}$$

A proper mathematical description of the global dynamics under varying structural states may then be obtained in the form of a VFP-ARX model.

The VFP-ARX(na, nb)_[pa, pb] model is of the following form [28]:

$$y_{\mathbf{k}}[t] + \sum_{i=1}^{na} a_i(\mathbf{k}) \cdot y_{\mathbf{k}}[t-i] = \sum_{i=0}^{nb} b_i(\mathbf{k}) \cdot x_{\mathbf{k}}[t-i] + e_{\mathbf{k}}[t] \quad (19)$$

$$e_{\mathbf{k}}[t] \sim \text{iid } \mathcal{N}(0, \sigma_e^2(\mathbf{k})) \quad \mathbf{k} \in \mathbb{R}^2 \quad (20)$$

$$E\{e_{k_{i,j}}[t] \cdot e_{k_{m,n}}[t-\tau]\} = \gamma_e[k_{i,j}, k_{m,n}] \cdot \delta[\tau] \quad (21)$$

with na, nb designating the AR and X order, respectively, $y_{\mathbf{k}}[t]$ the sensor's response signals, $x_{\mathbf{k}}[t]$ the exogenous excitation signals, and $e_{\mathbf{k}}[t]$ the model's residual (one-step-ahead prediction error) sequence, that is a white (serially uncorrelated) zero mean sequence with variance $\sigma_e^2(\mathbf{k})$. This may potentially be cross-correlated with its counterparts corresponding to different experiments (different \mathbf{k} 's). The symbol $E\{\cdot\}$ designates statistical expectation, $\delta[\tau]$ the Kronecker delta (equal to unity for $\tau = 0$ and equal to zero for $\tau \neq 0$), $\mathcal{N}(\cdot, \cdot)$ Gaussian distribution with the indicated mean and variance, and iid stands for identically independently distributed. The covariance of the residual series is designated as $\gamma_e[k_{i,j}, k_{m,n}]$, with $\gamma_e[k_{i,j}, k_{i,j}] = \sigma_e^2[k_{i,j}]$. All information in terms of interrelations among the data records is incorporated into the parameter estimation phase to obtain statistically optimal models.

The uniqueness of the VFP model structure is that the model parameters $a_i(\mathbf{k}), b_i(\mathbf{k})$ are modeled as explicit functions of the vector \mathbf{k} (which contains the damage magnitude and damage location components):

$$a_i(\mathbf{k}) = \sum_{j=1}^{pa} a_{i,j} \cdot G_j(\mathbf{k}) \quad b_i(\mathbf{k}) = \sum_{j=1}^{pb} b_{i,j} \cdot G_j(\mathbf{k}) \quad (22)$$

As Equation 22 indicates, the AR parameters $a_i(\mathbf{k})$ and the X parameters $b_i(\mathbf{k})$ are functions of the damage topology vector \mathbf{k} by belonging to pa, pb -dimensional functional subspace spanned by the mutually independent basis functions $G_1(\mathbf{k}), G_2(\mathbf{k}), \dots, G_p(\mathbf{k})$ (*functional basis*). The functional basis consists of polynomials of two variables (bivariate) obtained as tensor products from their corresponding univariate polynomials (Chebyshev, Legendre, Jacobi, and other families [28, 29]). The constants $a_{i,j}$ and $b_{i,j}$ designate the AR and X coefficients of projection to be estimated from the measured signals.

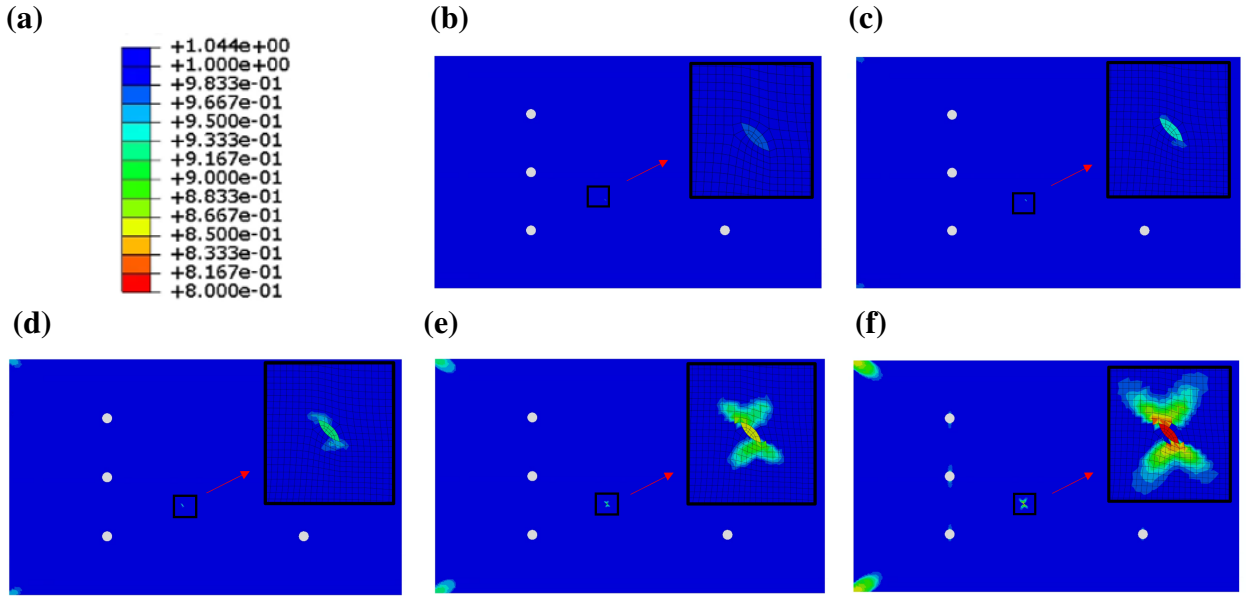


Fig. 1 Progressive damage analysis (PDA) with finite element (FE) model: (a) damage scale for PDA output (values represent a fraction of remaining element stiffness compared to the healthy state); (b) original 2 mm damage area (elements with reduced stiffness) within the healthy mesh; (c) 4 mm damage state after original damage area have propagated due to the tensile load; (d) 6 mm damage state after further propagation of the damage due to the tensile load; (e) 8 mm damage state after further propagation of the damage due to the tensile load; (f) Final 10 mm damage state after completion of the PDA simulation.

The estimation of damage states depends on an inverse optimization process that minimized the model prediction error with respect to the test signal over the damage parameter space \mathbf{K} , where $\mathbf{k} \in \mathbf{K}$. Residual sum-of-square is chosen as the loss function of this optimization process and shown below in Equation 23.

$$\hat{\mathbf{k}} = \arg \min_{\mathbf{k}} \{RSS(\mathbf{k} | u[t], y[t])\}, \quad RSS(\hat{\mathbf{k}} | u[t], y[t]) = \sum_{t=1}^N e^2[t, \hat{\mathbf{k}}] \quad (23)$$

In Equation 23, $u[t]$ and $y[t]$ are the test data. $y_{\mathbf{k}}[t]$ is the one-step-ahead prediction of the trained VFP-ARX model based on the test input data $u[t]$. The $\hat{\mathbf{k}}$ that minimizes the loss function is regarded as the closest estimation of the test damage case. Moreover, the confidence bound obtained from $\hat{\mathbf{k}}$ that follows the chi-squared distribution provides the probabilistic aspect of the damage estimation [3]. In a special case of the VFP-ARX model where the damage vector is a scalar, it is specified as the FP-ARX model. The detailed model identification process of the FP-ARX model can be found in [28].

III. The Simulations and Experimental Setup

A. Numerical Simulation of Progressive Damage Analysis

For performing progressive damage analysis with finite element modeling, the damage in the plate is initiated by specifying a 2 mm patch of elements to have degraded stiffness relative to the rest of the elements in the model. To propagate the damage, the plate is fixed at one end and a tensile load is applied on the other end.

As the damage propagates gradually, the material properties are recorded when the damaged area reaches sizes of 4 mm, 6 mm, 8 mm, and 10 mm. As a result, there are six material property states for the plate: healthy, the initial 2 mm damage size, and the four damage sizes recorded during the tensile test. The damaged states are illustrated in Figure 1. Any damage induced at the edges of the plate is caused by artificial high stresses due to boundary conditions.

The output of the PDA model is a FEM containing damaged states for the composite plate. The elements that are considered damaged by the PDA model, have reduced material properties representative of a damaged composite material. The composite plate used in the finite element simulation was composed of 16 plies. The material properties of each ply are shown in Table 1. The 16 plies are each 0.125 mm thick and oriented as [0 90 45 -45 -45 45 90 0 0 90 45 -45 -45 45 90 0]. The multi-physics FEM model has three components: composite plate, adhesive, and six PZT patches. The composite plate consists of 111,224 linear shell (S4) elements. The adhesive layers in between the plate and the sensors have 4,320 linear brick (C3D8) elements. The PZT patches are modeled by 2880 piezoelectric linear brick (C3D8E) elements.

Table 1 Composite material properties

Property	Value	Property	Value
E_{11}	143.7 GPa	ν_{23}	0.300
E_{22}	9.25 GPa	G_{12}	5.14 GPa
E_{33}	9.25 GPa	G_{13}	5.14 GPa
ν_{12}	0.372	G_{23}	3500 MPa
ν_{13}	0.372	ρ	1789 kg/m ³

B. Experimental Setup for Local and Global Damage Diagnosis

1. Composite UAV Wing Structure

Experiments were performed on a full-scale composite wing structure to investigate the integration of the VFP-based global SHM method and FS-TAR-based local SHM techniques. The sample composite structure was built on the design of the solar-powered UAV [30], which had a 120 inch wingspan and 12 inch cord length. The composite wing structure including skins and spars was manufactured using the wet-layup technique. All components were assembled using epoxy adhesives and cured at room temperature. The wing assembly had a total mass of 0.4 Kg and was sufficient to meet the designed loading requirements. By attaching incremental weights to the wing surface, it is possible to simulate the changes in the dynamics of the wing. This mimics different levels of reduced elasticity caused by incipient damages occurring over different locations on the wing structure [3]. A 2D damage topology was created over the wing surface at positions specified in Figure 2(c), which had a 2.5 inches increment in the cord direction and 6 inches increment in the span direction. Damage sizes ranged from 0 grams (no weights) (healthy state) to 15 grams (5 weights) with 3 grams increment. Each weight was attached to the specified location on the wing surface using adhesive wax (Figure 2(a)).

A 3 by 5 grid of accelerometer network was mounted on the wing surface as shown in Figure 2(a) and 2(b). The accelerometers were attached using Loctite 401 instant adhesive and were able to acquire high coherence signals up to 256 Hz. The accelerometer network covers the defined damage region and had an equidistant separation of 4 inches along the cord direction and 8 inches along the span direction (Figure 2(c)).

In order to acquire structural vibration response signals for subsequent damage detection, localization, and quantification, a vibration test was performed on the wing assembly clamped in a cantilever configuration. A DataPhysics V4 modal shaker was used with a stinger/impedance head (IH) assembly to excite the structure with broadband random actuation at the location shown in Figure 2(a). Sampling frequency was set to 512 Hz, which included high frequency modal response of the local structural components. At each damage state, 64 seconds of data were collected from 15 accelerometers and 1 impedance head (Force). Signal conditioner (PCB 483C28, gain = 0.2 ~ 200) was used to amplify signals to ~ 80% of channel scope range (1 V) on A/D module (DataPhysics abacus906).

In order to perform guided wave-based damage detection and identification, six lead zirconate titanate (PZT or piezoelectric) sensors (type PZT-5A, Acellent Technologies, Inc) of 6.35 mm (1/4 in) diameter and a thickness of 0.2 mm (0.0079 in) were attached to the composite UAV wing structure and cured for 24 hours in room temperature as shown in Figure 3(a). Note also the PZT sensor naming convention and the two damage locations L1 (location 1) and L2 (location 2 with the white cross mark) in Figure 3(a). Up to five three-gram weights were taped to the surface of the plate sequentially in damage locations 1 and 2, respectively to simulate local damage.

Actuation signals in the form of 5-peak tone bursts (5-cycle Hamming-filtered sine wave, 90 V peak-to-peak, 250 kHz center frequency) were generated in a pitch-catch configuration over each sensor consecutively. Data were collected

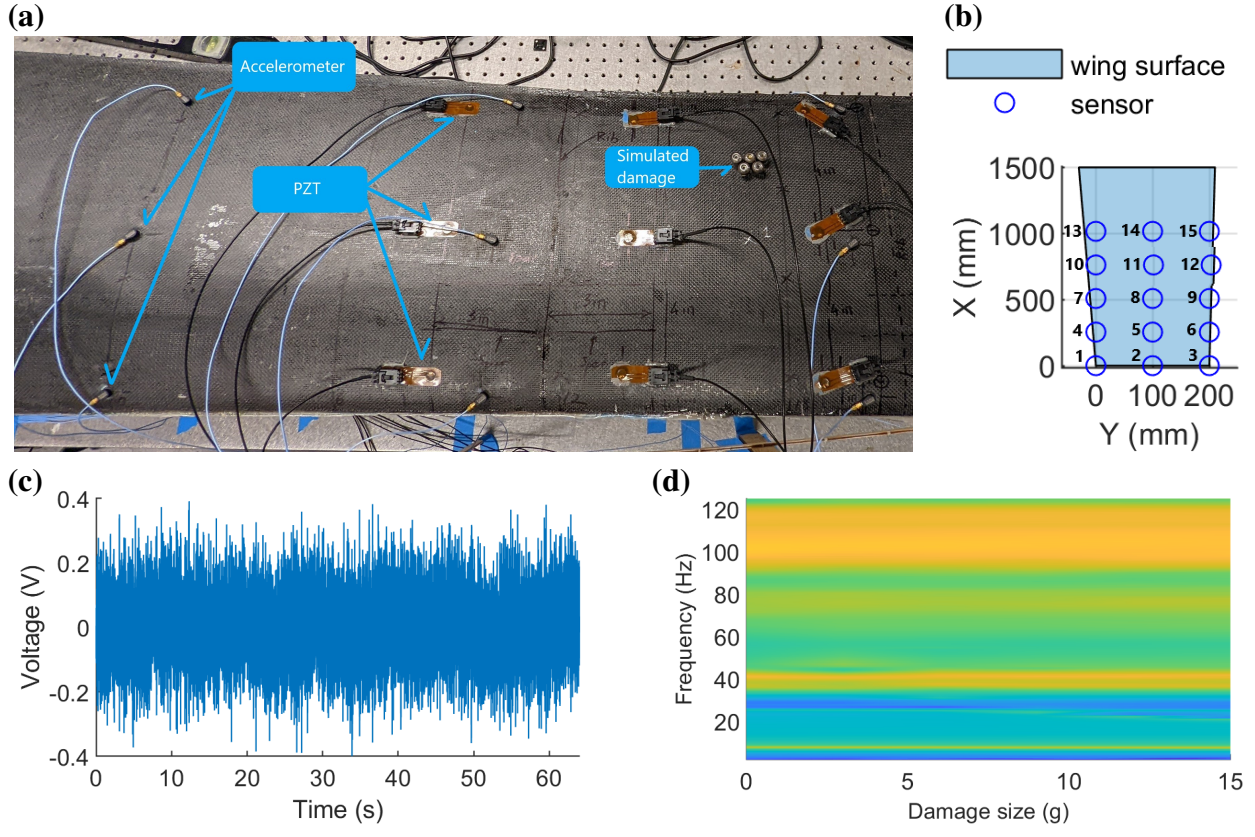


Fig. 2 Experimental setup for the vibration-based global damage diagnosis of the UAV wing: (a) accelerometers, simulated damages, and PZTs are installed on the UAV wing surface. The sensor location and numbering are shown in (b). The vibration signal from sensor 1 is shown in (c) and the non-parametric FRF of sensor 1 is indicated in (d) with respect to progressing damage size.

Table 2 Damage topology for the vibration-based damage diagnosis

Damage position ($k_{2,i}$)	Damage size ($k_{1,l}$)
$k_{2,0} = \text{location1}$	$k_{1,0} = 0\text{g}$ (healthy)
$k_{2,1} = \text{location2}$	$k_{1,1} = 3\text{g}$
—	$k_{1,2} = 6\text{g}$
—	$k_{1,3} = 9\text{g}$
—	$k_{1,4} = 12\text{g}$
—	$k_{1,5} = 15\text{g}$
Total number of experiments: 12 (2 baselines)	
Sampling frequency: $f_s = 512$ Hz, Signal bandwidth: [0 – 256] Hz	
Filter: Low-pass IIR, $f_{pass} = 125$ Hz, $f_{stop} = 128$ Hz	
Pass-band ripple: 1, Pass-band attenuation: 60	
Filter type: Chebyshev Type-II, Filtering method: <i>filtfilt</i>	
Signal length N in samples: Unfiltered signal: $N = 32\,768$ (64 s)	
Filtered signal: $N = 2\,816$ (11 s)	

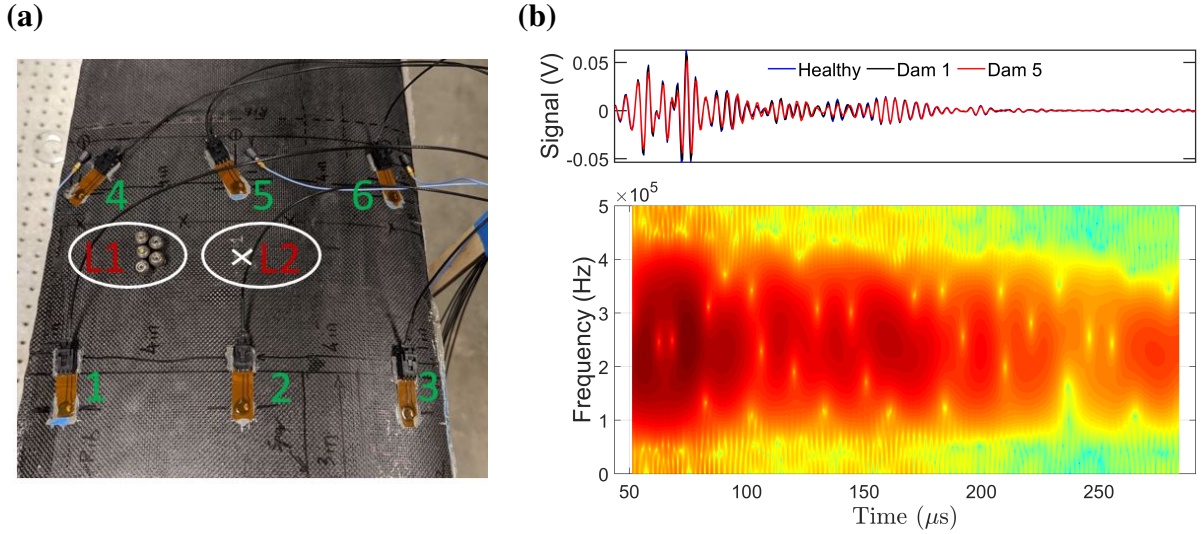


Fig. 3 Experimental setup of the guided wave-based local damage diagnosis of the same composite UAV wing: (a) The UAV wing retrofitted with the PZT sensors; (b) realization of the guided wave signals for healthy and damaged cases with a representative non-parametric spectrogram analysis.

using a ScanGenie III data acquisition system (Acellent Technologies, Inc) from selected sensors during each actuation cycle at a sampling frequency of 24 MHz. Five signals from each sensor (wave propagation path) and damage state were recorded. This led to a total of 30 data sets for each sensor. For the time-series modeling, the acquired signals were down-sampled to 2 MHz. This process resulted in 496-sample-long signals. Figure 3(b) presents indicative signal realization for different damage (health) state (top subplot) and non-parametric spectrogram of a single signal realization*.

IV. Experimental Assessment on a Composite UAV Wing

A. Local Diagnosis via FS-TAR Models

In the context of the active sensing guided wave-based local damage diagnosis methods, there are often multiple sensors installed in the area being monitored, and every actuator-sensor path in the network has to be examined to assess the integrity of the component. In the present study, Figure 3(a) shows the six actuator-sensor pairs retrofitted on the composite wing. There are two damaged locations, namely: location 1 (L1) and location 2 (L2). In this study, simulated damages have been used in the form of small weights mounted to the wing with tacky tapes.

Model selection of FS-TAR involves selecting the appropriate AR order na and functional subspaces \mathcal{F}_{AR} and \mathcal{F}_{σ_e} . In the present case, the best FS-TAR model minimizes the BIC criteria utilizing an integer optimization scheme as described in [22, 25]. The integer optimization scheme utilizes coarse optimization based on a genetic algorithm (population size 100, number of generations 100, crossover probability 0.8, and mutation probability 0.05) and fine optimization based on the concept of backward regression. In this study, the functional subspace considered was the wavelet basis function. In order to detect and identify damage in location 1 (L1), wave propagation signals from path 1-5 were considered for analysis. On the other hand, for damage diagnosis in location 2 (L2), wave propagation signals from path 2-5 were considered. For path 1-5 (location L1), the best model occurred for $na = 4$ and the functional subspaces are $\mathcal{F}_{AR} = \{G_1[t], G_3[t]\}$ ($pa = 2$) and $\mathcal{F}_{\sigma_e} = \{G_1[t], G_2[t]\}$ ($ps = 2$). This is compactly written as FS-TAR(4)_[2,2]. Similarly, for path 2-5 (location L2), the best model again occurred for $na = 4$ and $\mathcal{F}_{AR} = \{G_1[t], G_3[t]\}$ ($pa = 2$) and $\mathcal{F}_{\sigma_e} = \{G_1[t], G_2[t]\}$ ($ps = 2$) compactly written as FS-TAR(4)_[2,2]. The maximum-likelihood estimator was used for estimating the coefficients of projection vector ϑ .

Figure 4 shows the damage detection and identification results of the damage intersecting path 1-5 using the wavelet

*window length: 30 samples; 98% overlap; NFFT points: 30000 (zero-padding took place to obtain smooth magnitude estimates); frequency resolution $\Delta f = 666.66$ Hz.

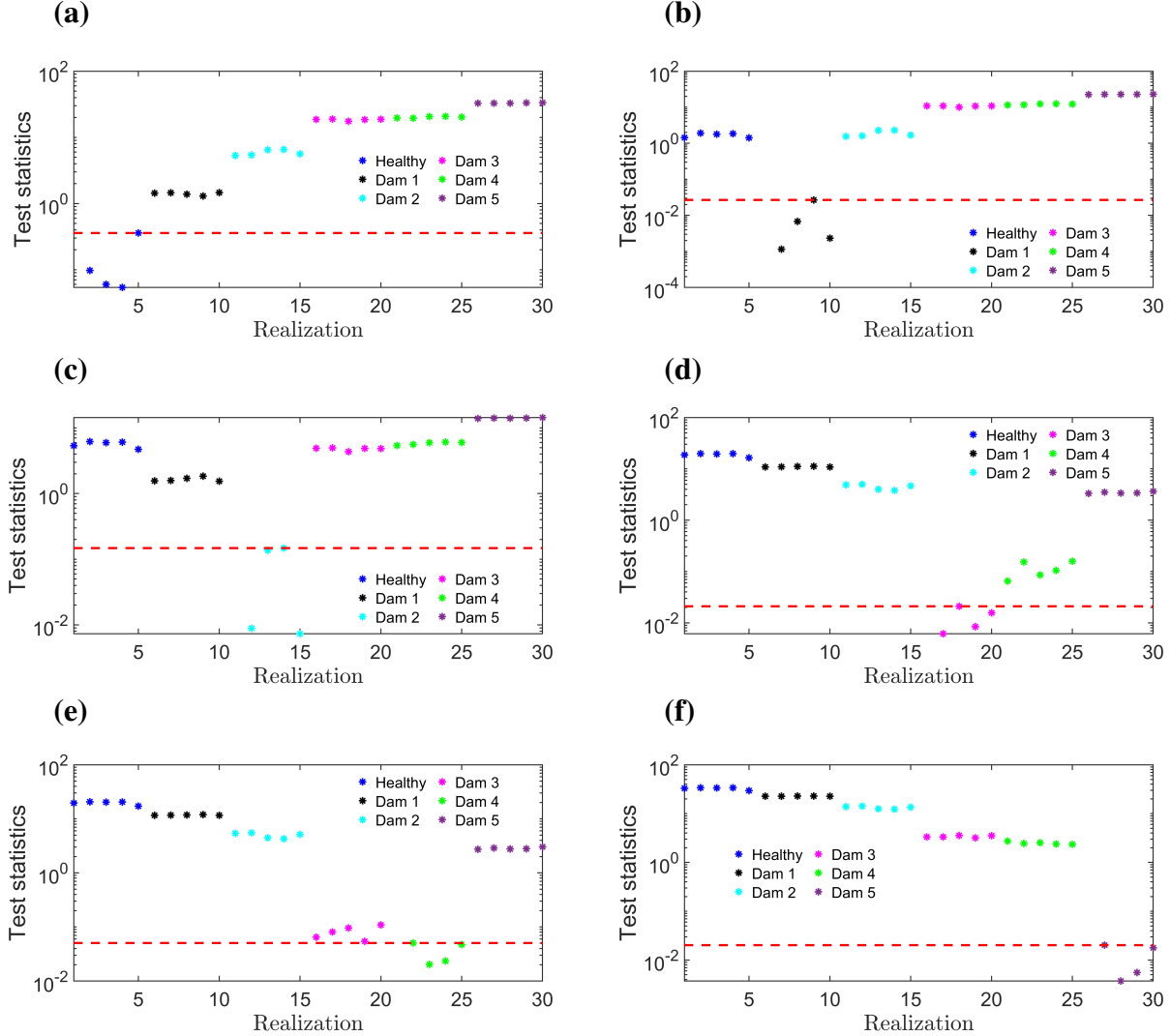


Fig. 4 Damage detection and identification results for the composite UAV wing using damage intersecting path 1-5 and the theoretical covariance matrix for damage location 1 (loc zero) : (a) damage detection; and identification of (b) damage level 1; (c) damage level 2; (d) damage level 3; (e) damage level 4; (f) damage level 5.

basis functions for damage location 1 (L1) using the theoretical formulation described in Section II.B.1. FS-TAR(4)_[2,2] model-based covariance matrix was used in estimating the characteristic quantity Q in Equation 14. Note that in Figure 4(a), all the healthy test statistics remain below the threshold (dotted red line), and test statistics for all other damage levels go outside the threshold. Figure 4(b)-(f) show the damage identification results for different damage levels, namely: damage level 1 (1 weight), damage level 2 (2 weights), damage level 3 (3 weights), damage level 4 (4 weights), and damage level 5 (5 weights). Note that perfect damage identification was achieved for all damage levels. For example, in Figure 4(e), test statistics for damage level 4 remain below the threshold, and all other structural states go beyond the threshold. The thresholds were manually adjusted in this case, as the α level gets close to 1. Similarly, Figure 5 shows the damage detection and identification results of the damage intersecting path 2-5 using the wavelet basis functions for damage location 2 (L2). Note that, in this case too, perfect damage detection and identification was achieved with no missed damage or damage misclassification.

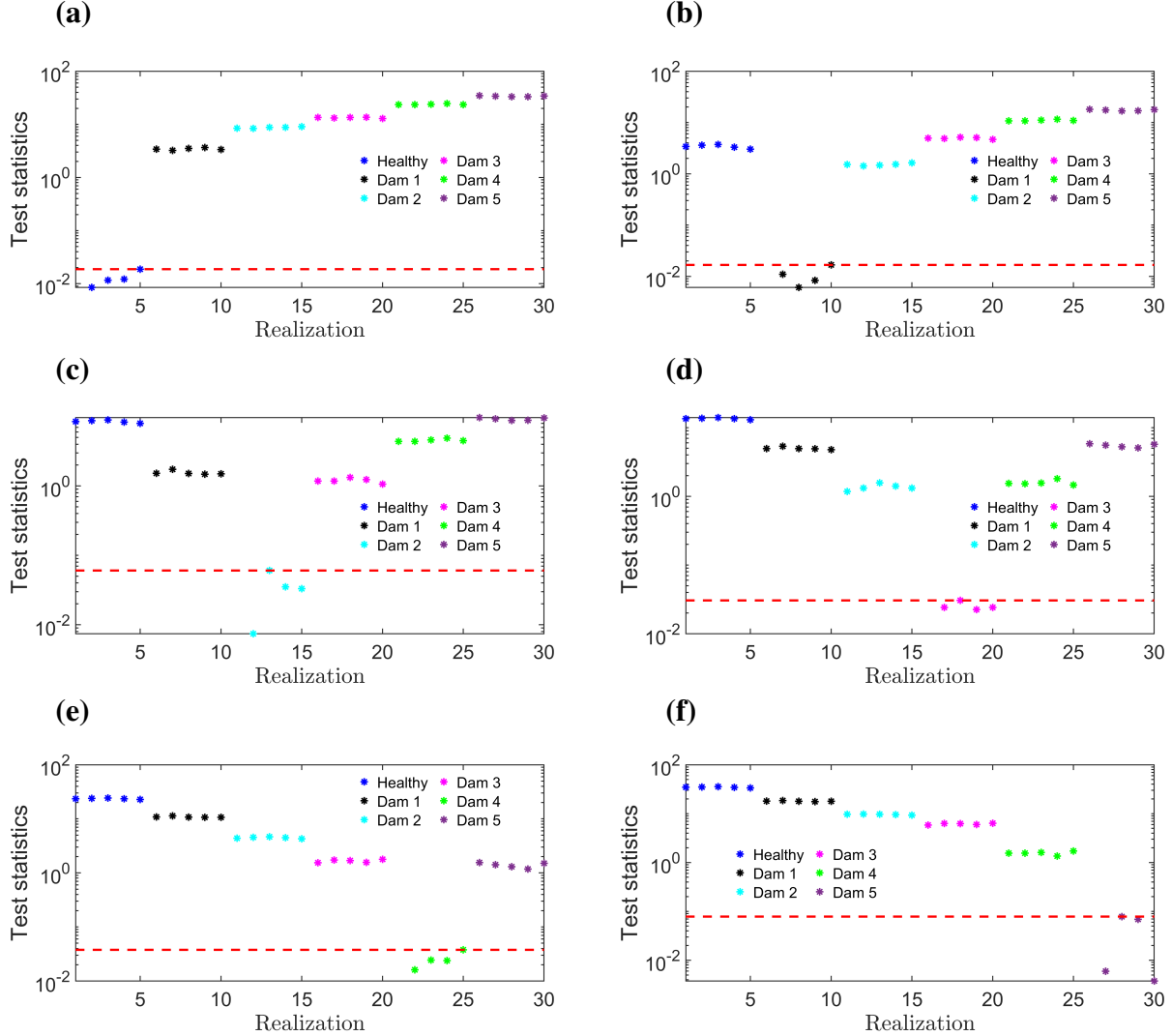


Fig. 5 Damage detection and identification results for the composite UAV wing using damage intersecting path 2-5 and the theoretical covariance matrix for damage location 2 (loc one) : (a) damage detection; and identification of (b) damage level 1; (c) damage level 2; (d) damage level 3; (e) damage level 4; (f) damage level 5.

B. Global Diagnosis via FP-ARX models

Within the VFP-ARX framework of vibration-based global damage diagnosis, an FP-ARX model, which is a VFP-ARX model with $\text{dim}(k) = 1$, can be used to estimate the progression of damage magnitude at a predetermined location of the structure. The exact damage topology used in the guided wave-based local damage diagnosis (with the help of the FS-TAR model) is also used for the vibration-based global damage diagnosis (with the help of FP-ARX model), which includes 2 damage locations, namely: location 1 (L1) and location 2 (L2), and each with 5 damage levels, namely: damage level 1 (1 weights, 3 grams), damage level 2 (2 weights, 6 grams), damage level 3 (3 weights, 9 grams), damage level 4 (4 weights, 12 grams), damage level 5 (5 weights, 15 grams).

The FP-ARX model was trained on the signal acquired from sensor 1 specified in Figure 2(c). A data segment of 11 seconds was selected from 64 seconds of the vibration response signal. The model selection was performed by minimizing the Bayesian Information Criterion (BIC) and RSS/SSS over the defined range of $n \in [2, 70]$, $p \in [1, 6]$ and is shown in Figure 6. The best model occurred for $na = 61$, $nb = 61$ and $p = 6$.

The residual-based damage estimation process was then performed using the trained FP-ARX model. Test data was created from a non-overlapping signal segment of 11 seconds. Then the inverse optimization process minimized the residuals of the model prediction with respect to the damage magnitude parameter $k^1 \in [0, 15]$ grams. The results of the

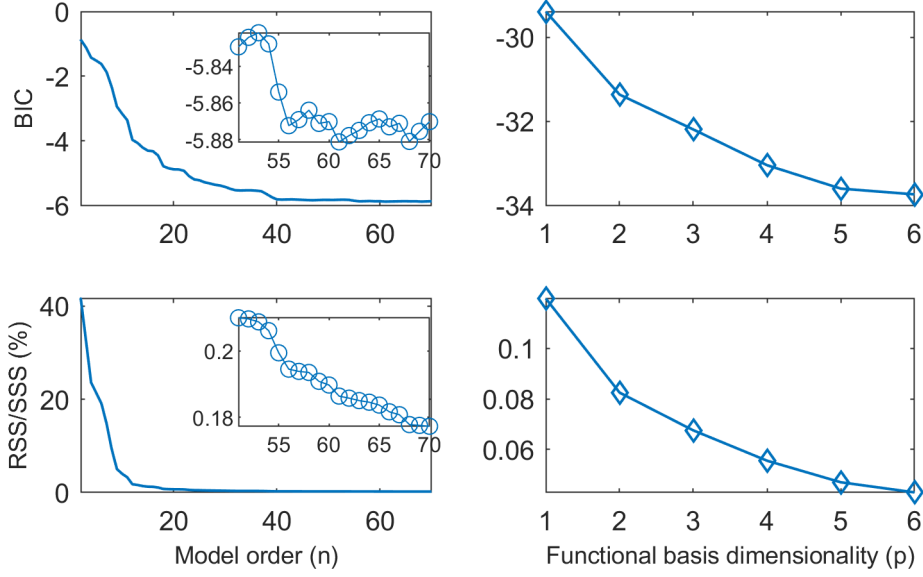


Fig. 6 Model order and functional basis dimensionality selection process of the FP-ARX model: both the percent RSS/SSS and the BIC criteria are utilized.

estimation for different damage levels are shown in Figure 7 and Figure 8 for locations 1 and 2, respectively.

The estimation of each damage case had an error of $\epsilon \leq 1$ gram, which shows acceptable estimation accuracy. On the other hand, the estimated damage value falls outside the confidence interval in Figure 7(c), (d), (e) and Figure 8(a), (c), (d), and (e). This shows that the model loses its generalizability when opting for accuracy. A special case is shown in Figure 7(d), where the estimation error is 1.953 grams. In this case, the estimated damage level drifts from level 3 (9 grams) to level 4 (12 grams) showing that the reconstructed signal is close to RSS space. The cause of this confusion could come from the non-uniqueness of the dynamic changes induced by the damage.

C. Comparison Between Local and Global Methods

In this section, the comparison of the local guided wave-based and the global vibration-based methods is addressed with respect to their respective damage diagnosis capability. A quantitative assessment is attempted regarding the damage size that can be perfectly detected and identified by these two methods.

Note that for the case of the vibration-based damage diagnosis, in Figure 7(c), (d), (e) for location 1 (L1) based on sensor 1, the estimation of the corresponding damage size falls outside the 99% confidence intervals (CIs), although the point estimates are quite accurate. This is due to the narrow estimation CIs obtained via the FP-ARX diagnostic method. The FP-ARX allows for accurate damage size estimation with the potential drawback of narrow CIs that do not include the point estimates. However, as can be observed in Figures 7(a), (b) and (f), where the damage magnitude is 0 (healthy), 3, and 15 grams (highest damage size for this case), respectively, the estimation of the corresponding damage sizes is very accurate. When it comes to the results presented in Figure 8 for position 2 (L2) and sensor 1, it can be observed that the FP-ARX method exhibits somewhat reduced accuracy, as the damage size estimates fall outside the CIs in all cases apart from Figure 8(f), that corresponds to the largest damage size, where the estimation is accurate. The reduced accuracy of the global method for damage location 2 can be attributed to the distance of sensor 1 from damage location 2: sensor 1 is closer to damage location 1 than location 2, therefore the diagnostic results for location 1 appear more accurate and robust compared to the corresponding results obtained for location 2 when using signals collected from sensor 1.

For the case of the ultrasonic guided wave-based local method, the specific damage sizes that are not accurately quantified by the vibration-based method, can be accurately identified, as shown in Figure 4(c), (d), (e), for location 1 (L1), and Figure 5(c), (d), and (e) for location 2 (L2), using damage intersecting paths 1-5 and 2-5, respectively. Therefore, proper selection of the actuator-sensor path is necessary to capture small variations in damage level/size as wave propagation paths that intersect with the location of damage show increased sensitivity for smaller damage sizes

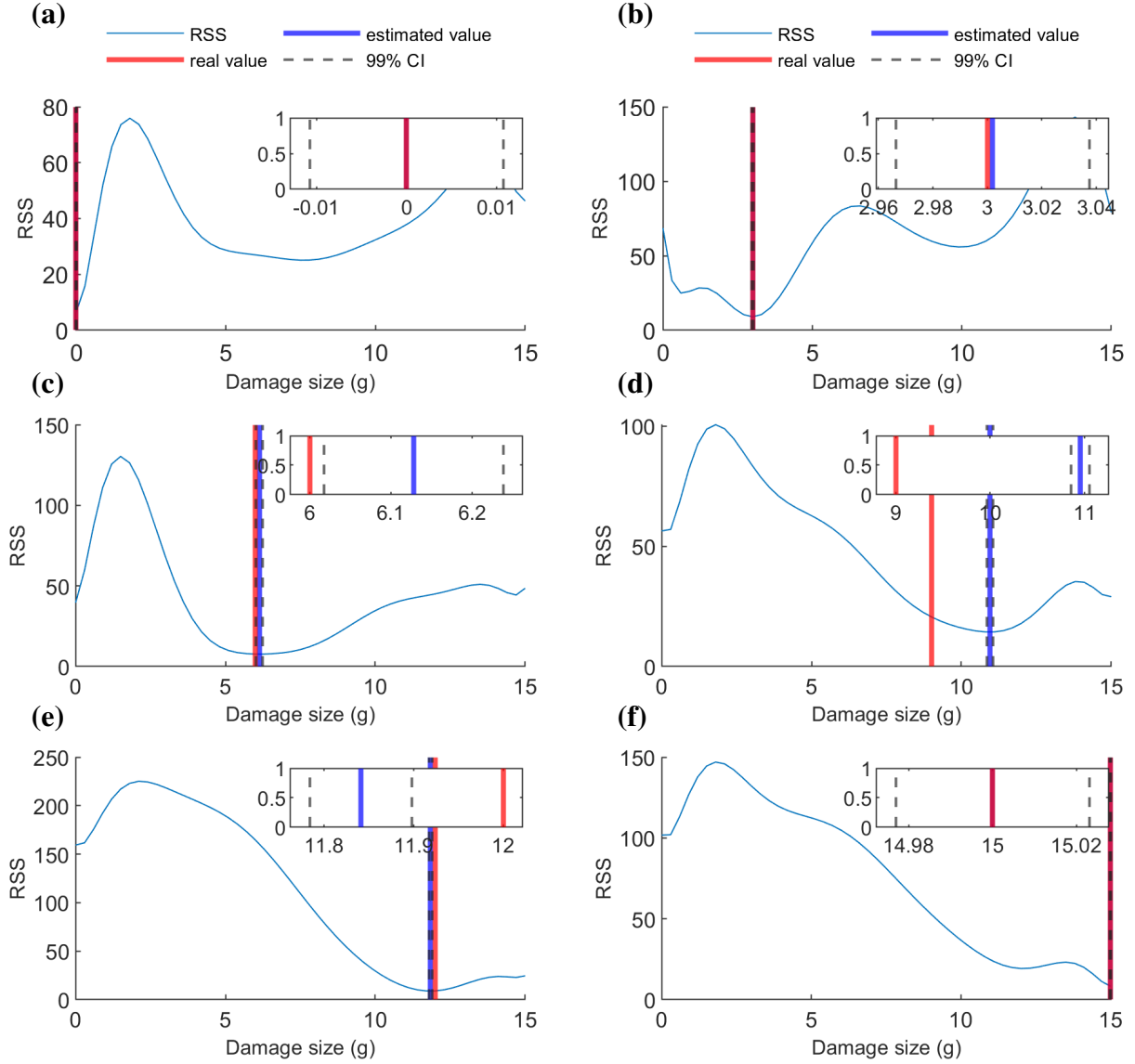


Fig. 7 Residual-based inverse estimation of the damage magnitude using FP-ARX(61, 61)_{6,6} trained on sensor 1 for progressing damage at location 1 within the region covered by the PZT network. The series of damage includes (a) healthy (0 gram), (b) damage level 1 (3 grams), (c) damage level 2 (6 grams), (d) damage level 3 (9 grams), (e) damage level 4 (12 grams) and (f) damage level 5 (15 grams). A 99% confidence interval is given with each damage estimation.

(see [11]).

V. Numerical Assessment for Progressive Damage Analysis on a Composite Plate

Figure 9 shows the FEM model, model's sensor layout, representative healthy and damaged signals, and the non-parametric spectrogram for a representative signal realization [†].

[†]window length: 30 samples; 98% overlap; NFFT points: 30000 (zero-padding took place to obtain smooth magnitude estimates); frequency resolution $\Delta f = 666.66$ Hz.

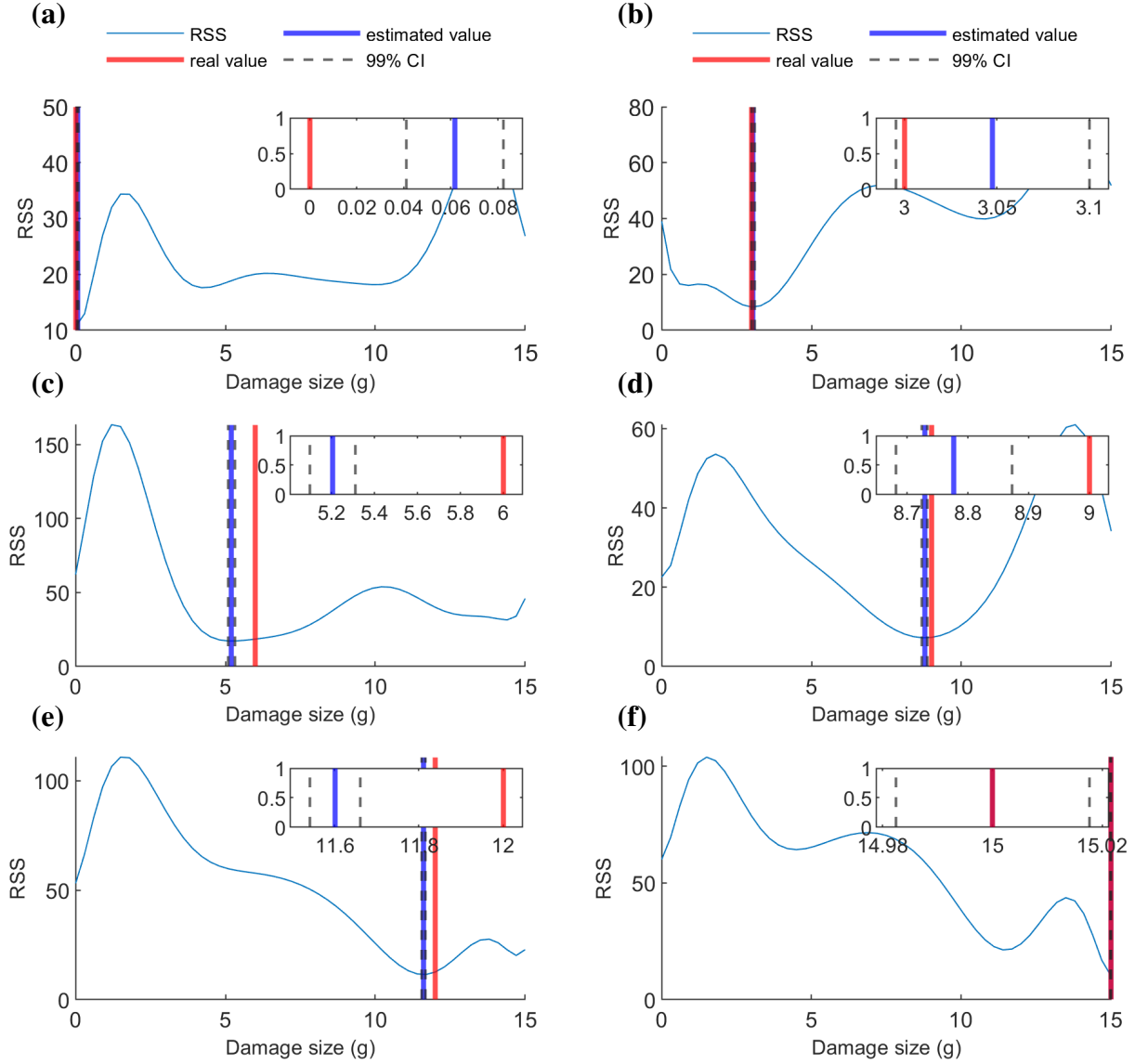


Fig. 8 Residual-based inverse estimation of the damage magnitude using $\text{FP-ARX}(61,61)_{6,6}$ model trained on sensor 1 for progressing damage at location 2 within the region covered by the PZT network. The series of damage includes (a) healthy (0 gram), (b) damage level 1 (3 grams), (c) damage level 2 (6 grams), (d) damage level 3 (9 grams), (e) damage level 4 (12 grams) and (f) damage level 5 (15 grams). A 99% confidence interval is given with each damage estimation.

During the progressive damage analysis of the composite plate, ultrasonic guided wave signals were acquired from the Lead Zirconate Titanate (PZT) sensors mounted on the composite plate. Sensor 1, as shown in Figure 9(b), acts as an actuator. A 5-peak tone burst actuation with a center frequency of 250 kHz was applied at sensor 1 as an actuation signal. The response signal was received from sensors 4, 5, and 6 for healthy, 2 mm damage, 4 mm damage, 6 mm damage, 8 mm damage, and 10 mm damage of the composite plate.

Figure 10 shows the plot of percent root mean squared error (RMSE) values for different damage levels. Ultrasonic guided wave signals were received from different structural states namely: healthy, damage level 1 (2 mm damage), damage level 2 (4 mm damage), damage level 3 (6 mm damage), damage level 4 (8 mm damage), and damage level 5

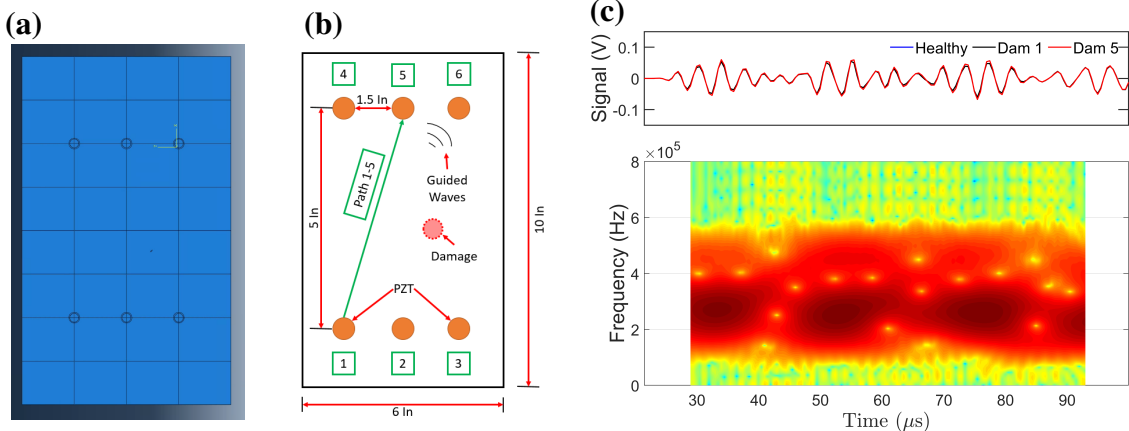


Fig. 9 (a) Multiphysics FEM model in Abaqus; (b) the model's sensor layout and dimension; (c) indicative response signals from the PZT sensor for different damage levels and a representative non-parametric spectrogram.

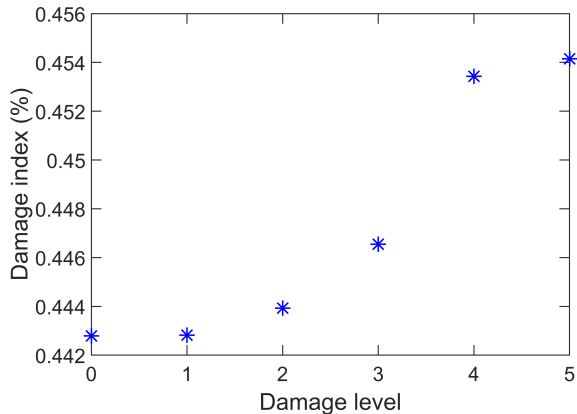


Fig. 10 Damage index plot for the signals from path 1-5: shows how damage indices change with the increase in damage level in the composite plate for progressive damage analysis.

(10 mm damage) for path 1-4, 1-5 and 1-6. Here, the RMSE values from path 1-5 have been presented. Note that the percent RMSE values obtained from path 1-5 gradually increase for damage level 1, 2, and 3. For damage level 4, the RMSE value increase sharply, and for damage level 5, a slight increase in RMSE value can be observed.

The frequency response of the composite plate was also recorded at each damage size during the progressive damage analysis. All major modal frequencies in the 0 Hz to 1000 Hz range were recorded, and Table 3 compares the frequencies of the healthy and different damaged states. The natural frequencies of the major modes do not change for the healthy case, damage level 1 (2 mm), and damage level 2 (4 mm) for most of the modes. The reason is that with 2 mm and 4 mm damage size, the vibration characteristic of the structure does not change to an appreciable amount as the size of the damage is small. However, for 6 mm, 8 mm and 10 mm damage size, the natural frequencies change slightly.

Figure 11(a) shows the magnitude of the frequency response function from 0-1000 Hz for different damage levels from sensor 2. Note that the FRF changes as the size (level) of the damage increases. Figure 11(b) shows a zoomed in view of the FRF peak at 191.5 Hz. Note that for healthy, 2 mm damage, and 4 mm damage the FRF is almost the same. However, for 8 mm and 10 mm damage, the FRF magnitude decreases gradually with the increase in damage size. In Figure 11(c), the zoomed in view of the peak at 505 Hz, with the increase in damage size, the FRF magnitude changes, however, they do not follow any specific trend.

Table 3 Change of natural frequencies with different damage levels

Mode	Healthy	2 mm	4 mm	6 mm	8 mm	10mm
Mode 1 (Hz)	169.37	169.37	169.37	169.36	169.34	169.32
Mode 2 (Hz)	191.57	191.57	191.57	191.57	191.55	191.54
Mode 3 (Hz)	395.11	395.11	395.11	395.10	395.04	395.00
Mode 4 (Hz)	504.9	504.9	504.89	504.89	504.81	504.76
Mode 5 (Hz)	521.42	521.42	521.42	521.41	521.32	521.26
Mode 6 (Hz)	622.13	622.13	622.13	622.12	622.02	621.95
Mode 7 (Hz)	740.56	740.56	740.56	740.55	740.46	740.40
Mode 8 (Hz)	877.41	877.41	877.40	877.38	877.24	877.15

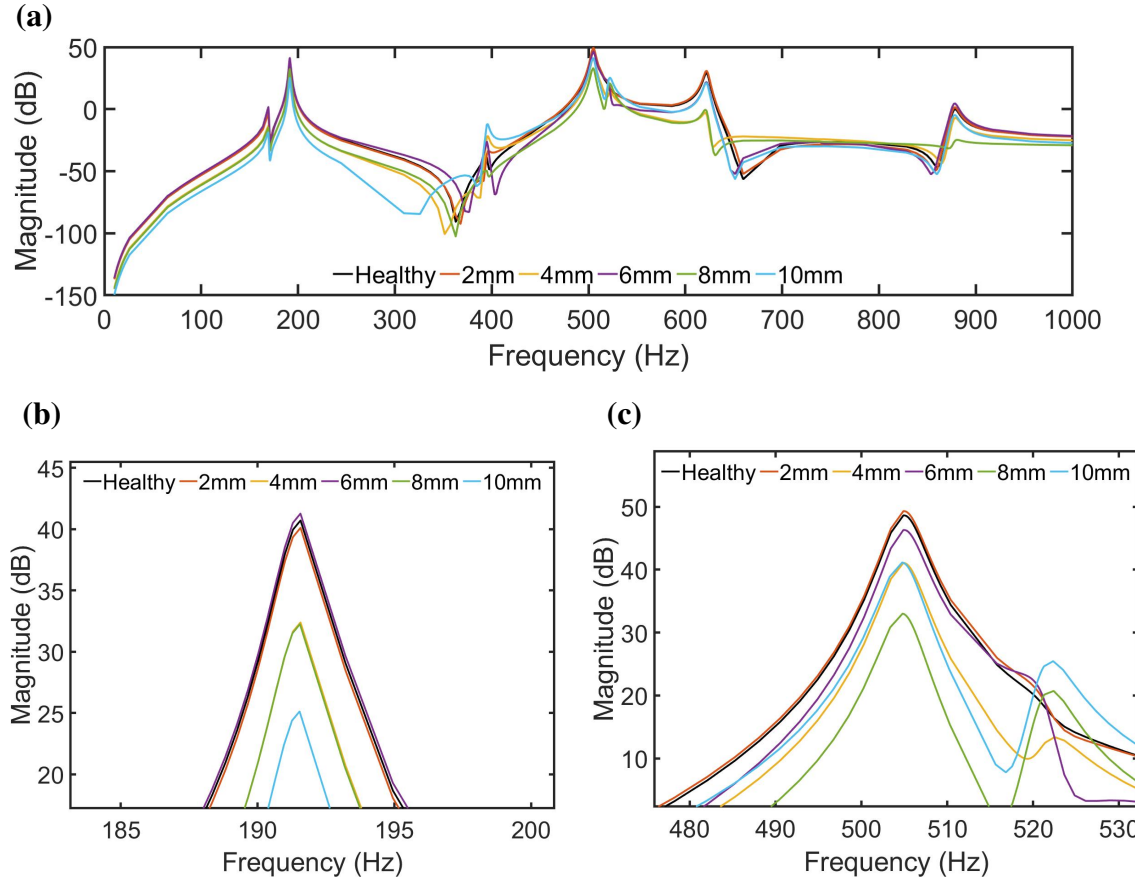


Fig. 11 Frequency response function (FRF) for different damage levels from progressive damage analysis of the composite plate from FE model: (a) frequency response functions from 0-1000 Hz for different damage levels; (b) zoomed in view of the FRF magnitude at 191.5 Hz.; (c) zoomed in view of the FRF magnitude at 505 Hz.

VI. Concluding Remarks

The objective of this paper was to explore and evaluate two different SHM approaches, namely a guided wave-based local damage diagnosis and a vibration-based global damage diagnosis scheme. The methods were addressed within a unified stochastic time series modeling and diagnostic framework. FS-TAR models, which are stochastic time-varying models, were used to model the guided wave propagation signals from the progressive damage analysis of the composite

plate and the UAV wing structure. It was shown that the local guided wave-based damage diagnosis scheme can detect and identify damage as small as 2 mm and successive progression of damage after that from the numerical simulation of the progressive damage analysis. Guided wave signals received from the experimental setup of the UAV wing structure can successfully detect and identify damage as small as 3 grams with the FS-TAR model-based damage diagnosis scheme. Then, FP-ARX models, which are stochastic global models for global vibration analysis, were used for vibration-based global damage diagnosis on the same composite wing structure. The VFP/FP-ARX model estimates the global damage by minimizing the residual sum of squares of the model prediction parametrized with respect to the damage size. It was shown that the global method can effectively detect damage over the entire structure with a carefully selected sensor. However, the VFP/FP-ARX model-based method may encounter difficulties in accurately estimating the damage magnitude/size for cases where the obtained damage size estimation confidence intervals are too narrow. The FS-TAR models, on the other hand, show great accuracy and robustness in identifying and quantifying damage in a local region when a proper selection of wave propagation paths has taken place. As a result, the integration of these two methods within a stochastic time series framework has the potential to enhance the overall performance and robustness with respect to damage diagnosis.

Acknowledgments

This work is supported by the U.S. Air Force Office of Scientific Research (AFOSR) grant “Formal Verification of Stochastic State Awareness for Dynamic Data-Driven Intelligent Aerospace Systems” (FA9550-19-1-0054) with Program Officer Dr. Erik Blasch.

References

- [1] Doebling, S., Farrar, C., and Prime, M., “A summary review of vibration-based damage identification methods,” *Shock and Vibration Digest*, Vol. 30, No. 2, 1998, pp. 91–105.
- [2] Ihn, J.-B., and Chang, F.-K., “Pitch-catch Active Sensing Methods in Structural Health Monitoring for Aircraft Structures,” *Structural Health Monitoring*, Vol. 7, No. 1, 2008, pp. 5–19. <https://doi.org/10.1177/1475921707081979>.
- [3] Kopsaftopoulos, F. P., and Fassois, S. D., “A functional model based statistical time series method for vibration based damage detection, localization, and magnitude estimation,” *Mechanical Systems and Signal Processing*, Vol. 39, No. 1-2, 2013, pp. 143–161.
- [4] Amer, A., and Kopsaftopoulos, F. P., “On leveraging network-wide information from hotspot sensor networks using Multi-output Gaussian Process regression models,” *Proceedings of the Vertical Flight Society 77th Annual Forum & Technology Display*, 2021.
- [5] Zhuang, Y., Kopsaftopoulos, F., Dugnani, R., and Chang, F.-K., “Integrity monitoring of adhesively bonded joints via an electromechanical impedance-based approach,” *Structural Health Monitoring*, Vol. 17, No. 5, 2018, pp. 1031–1045.
- [6] Sodano, H. A., “Development of an automated eddy current structural health monitoring technique with an extended sensing region for corrosion detection,” *Structural Health Monitoring*, Vol. 6, No. 2, 2007, pp. 111–119.
- [7] Roy, S., Lonkar, K., Janapati, V., and Chang, F.-K., “A novel physics-based temperature compensation model for structural health monitoring using ultrasonic guided waves,” *Structural Health Monitoring*, Vol. 13, No. 3, 2014, pp. 321–342.
- [8] Janapati, V., Kopsaftopoulos, F., Li, F., Lee, S. J., and Chang, F.-K., “Damage detection sensitivity characterization of acousto-ultrasound-based structural health monitoring techniques,” *Structural Health Monitoring*, Vol. 15, No. 2, 2016, pp. 143–161.
- [9] Ahmed, S., and Kopsaftopoulos, F., “Stochastic Identification of Guided Wave Propagation under Ambient Temperature via Non-Stationary Time Series Models,” *Sensors*, Vol. 21, No. 16, 2021. URL <https://www.mdpi.com/1424-8220/21/16/5672>.
- [10] Amer, A., Ahmed, S., and Kopsaftopoulos, F., “Active-Sensing Structural Health Monitoring via Statistical Learning: An Experimental Study Under Varying Damage and Loading States,” *European Workshop on Structural Health Monitoring*, Springer, 2020, pp. 456–468.
- [11] Amer, A., and Kopsaftopoulos, F. P., “Statistical guided-waves-based structural health monitoring via stochastic non-parametric time series models,” *Structural Health Monitoring*, 2021, pp. 1–28.

- [12] Ahmed, S., and Kopsaftopoulos, F., “Active sensing acousto-ultrasound SHM via stochastic time series models,” *Health Monitoring of Structural and Biological Systems XVI*, Vol. 12048, SPIE, 2022, pp. 358–366.
- [13] Kopsaftopoulos, F., and Fassois, S., “Vibration based health monitoring for a lightweight truss structure: experimental assessment of several statistical time series methods,” *Mechanical Systems and Signal Processing*, Vol. 24, No. 7, 2010, pp. 1977–1997.
- [14] Ahmed, S., and Kopsaftopoulos, F., “Investigation of Broadband High-Frequency Stochastic Actuation for Active-Sensing SHM Under Varying Temperature,” *International Workshop on Structural Health Monitoring, Stanford University, USA*, 2019.
- [15] Ahmed, S., and Kopsaftopoulos, F., “Statistical Active-Sensing Structural Health Monitoring via Stochastic Time-Varying Time Series Models,” *2022 American Control Conference (ACC)*, IEEE, 2022, pp. 3599–3606.
- [16] Ahmed, S., and Kopsaftopoulos, F., “Active Sensing Acousto-Ultrasound SHM via Stochastic Non-stationary Time Series Models,” *European Workshop on Structural Health Monitoring: EWSHM 2022-Volume 2*, Springer, 2022, pp. 256–266.
- [17] Spada, A., Capriotti, M., and Lanza di Scalea, F., “Global-local model for three-dimensional guided wave scattering with application to rail flaw detection,” *Structural Health Monitoring*, 2021.
- [18] Zhu, Y., Li, F., and Bao, W., “Fatigue crack detection under the vibration condition based on ultrasonic guided waves,” *Structural Health Monitoring*, Vol. 20, No. 3, 2021, pp. 931–941.
- [19] Klepka, A., Staszewski, W. J., Jenal, R., Szwedo, M., Iwaniec, J., and Uhl, T., “Nonlinear acoustics for fatigue crack detection—experimental investigations of vibro-acoustic wave modulations,” *Structural Health Monitoring*, Vol. 11, No. 2, 2012, pp. 197–211.
- [20] Liu, B., Luo, Z., and Gang, T., “Influence of low-frequency parameter changes on nonlinear vibro-acoustic wave modulations used for crack detection,” *Structural Health Monitoring*, Vol. 17, No. 2, 2018, pp. 218–226.
- [21] Ooijevaar, T., Rogge, M. D., Loendersloot, R., Warnet, L., Akkerman, R., and Tinga, T., “Vibro-acoustic modulation-based damage identification in a composite skin-stiffener structure,” *Structural health monitoring*, Vol. 15, No. 4, 2016, pp. 458–472.
- [22] Poulimenos, A., and Fassois, S., “Parametric time-domain methods for non-stationary random vibration modelling and analysis—a critical survey and comparison,” *Mechanical systems and signal processing*, Vol. 20, No. 4, 2006, pp. 763–816.
- [23] Sotiriou, D., Kopsaftopoulos, F., and Fassois, S., “An adaptive time-series probabilistic framework for 4-D trajectory conformance monitoring,” *IEEE Transactions on Intelligent Transportation Systems*, Vol. 17, No. 6, 2016, pp. 1606–1616.
- [24] Ljung, L., *System Identification: Theory for the User*, 2nd Edition, Prentice-Hall, Hoboken, NJ, 1999.
- [25] Spiridonakos, M., and Fassois, S., “An FS-TAR based method for vibration-response-based fault diagnosis in stochastic time-varying structures: experimental application to a pick-and-place mechanism,” *Mechanical Systems and Signal Processing*, Vol. 38, No. 1, 2013, pp. 206–222.
- [26] Ahmed, S., “Data-driven stochastic modeling of guided wave propagation and robust damage diagnosis,” PhD Dissertation, Department of Mechanical, Aerospace and Nuclear Engineering, Rensselaer Polytechnic Institute, USA, 2022.
- [27] Sakellariou, J. S., and Fassois, S. D., “Functionally Pooled Models for The Global Identification of Stochastic Systems Under Different Pseudo-Static Operating Conditions,” *Mechanical Systems and Signal Processing*, Vol. 72-73, No. 5, 2016, p. 785–807. <https://doi.org/10.1016/j.ymssp.2015.10.018>.
- [28] Kopsaftopoulos, F. P., “Advanced Functional and Sequential Statistical Time Series Methods for Damage Diagnosis in Mechanical Structures,” PhD Dissertation, Department of Mechanical Engineering & Aeronautics, University of Patras, Patras, Greece, January 2012.
- [29] Kopsaftopoulos, F. P., and Fassois, S. D., “Vector-Dependent Functionally Pooled ARX Models for the Identification of Systems Under Multiple Operating Conditions,” *Proceedings of the 16th IFAC Symposium on System Identification, (SYSID)*, Elsevier, Brussels, Belgium, 2012, pp. 105–117.
- [30] Arumbakkam, S., Brassard, K., Casey, P., Fahey, L., Hoddinott, D., Khan, T., Liu, E., Lou, Z., Moncton, M., Olins, Y., et al., “Design of an Intelligent Self-Aware Solar-Powered Unmanned Aerial Vehicle: Conventional and Unconventional Design Approaches,” *AIAA Scitech 2019 Forum*, 2019, p. 0316.